

Evolution of X-ray irradiation during the 1999–2000 outburst of the black hole binary XTE J1859 + 226

Mariko Kimura^{1,2★} and Chris Done²

¹*Department of Astronomy, Graduate School of Science, Kyoto University, Oiwakecho, Kitashirakawa, Sakyo-ku, Kyoto 606-8502, Japan*

²*Department of Physics, University of Durham, South Road, Durham DH1 3LE, UK*

Accepted 2018 October 3. Received 2018 September 28; in original form 2018 August 1

ABSTRACT

X-ray irradiation in X-ray binaries is thought to control the behaviour at the outer disc, which is observable mainly at optical wavelengths. It is generally parametrized phenomenologically, but it can also be predicted from theoretical models of irradiated discs and their coronae/winds. We test these models using five multiwavelength *Hubble Space Telescope* and quasi simultaneous *Rossi X-Ray Timing Explorer (RXTE)* data sets from the black hole binary XTE J1859 + 226. These show how the reprocessed optical emission changes during outburst as the source fades from the very high/intermediate state at $\sim 0.4L_{\text{Edd}}$ down through the high/soft state towards the transition to the hard state at $\sim 0.02L_{\text{Edd}}$. The models are able to reproduce the small change in reprocessing efficiency as the source flux decreases by a factor of two, and the spectrum softens from the very high/intermediate state to the bright high/soft state. However, the low luminosity high/soft state as well as the transition spectrum show more complex behaviour that is not well described by current models. We suggest the disc geometry has changed drastically during the outburst, probably due to tidal forces, and that the disc is no longer in steady state at the late stage of the outburst.

Key words: accretion, accretion discs – black hole physics – stars: individual (XTE J1859 + 226) – X-rays: binaries.

1 INTRODUCTION

Low-mass X-ray binaries (LMXBs) have a black hole or a neutron star as a central object with a companion low-mass star which fills its Roche lobe. Mass transfer takes place, forming an accretion disc around the central object, and this disc is globally unstable if it crosses the Hydrogen ionization temperature at any radius. The disc then cycles between long quiescent intervals punctuated by dramatic outbursts, with fast rise and exponential decay, during which most of the disc material is accreted (e.g. Tanaka & Shibazaki 1996; Chen, Shrader & Livio 1997). This is rather different to the classic disc instability mechanism as first outlined to describe normal dwarf-nova-type outbursts, which show rapid decline (Osaki 1996, for a review). In this kind of outbursts, the H-ionization triggers a heating wave which sweeps across the disc, but the outer disc soon dips below the H-ionization temperature, triggering a cooling wave which switches the disc back to quiescence. The major difference in behaviour between LMXBs and dwarf novae is that the central accretion flow is much brighter than in dwarf novae due to the higher gravitational potential of the central object. X-ray irradiation from the inner disc is then important, heating the outer disc, and

preventing Hydrogen recombination from launching the cooling wave which switches off the outburst. Such irradiation controlled decays generally match well to the observed light curves in LMXBs (Mineshige & Wheeler 1989; King & Ritter 1998; King 1998; Dubus, Hameury & Lasota 2001; Lasota 2001; Coriat, Fender & Dubus 2012).

X-ray irradiation of the outer disc should be directly observable, as it produces reprocessed optical (van Paradijs & McClintock 1994; de Jong, van Paradijs & Augusteijn 1996). It also produces a hot disc atmosphere/wind due to another ionization instability which operates for material in pressure balance (here, hydrostatic equilibrium). X-rays heat the surface, so it expands, and its density decreases, and its ionization state increases so that it can be almost completely ionized. Deeper down, the material must have larger pressure in order to support the weight of the upper layers, and then, its density must increase. Bremsstrahlung cooling becomes more important, reducing the temperature, hence increasing the density to remain in pressure balance. This decreases the ionization state so that bound transitions can exist, and line cooling dramatically decreases the temperature. This leads to a sharp transition between a highly ionized atmosphere, heated to the Compton temperature, and a much more neutral disc photosphere (Krolik & Kallman 1982). The sound speed c_s of the heated atmosphere gives a typical height of $H \sim c_s/v_\phi(R)$, where v_ϕ is the Keplerian velocity of the disc, and produces a wind where

* E-mail: mkimura@kusastro.kyoto-u.ac.jp

$c_s > v_{\text{esc}}(R) \sim v_\phi(R)$ (Begelman, McKee & Shields 1983; Woods et al. 1996; Done, Tomaru & Takahashi 2018).

Hence, the signatures of an irradiated outer disc are a highly ionized X-ray atmosphere/wind, reprocessed optical emission, and long decays of outbursts. However, there is as yet no detailed modelling of these effects and their observational tests. For example, the best calculations of disc-instability model first used the standard (unilluminated) disc models. These predicted that the outer regions of the disc are self-shielded (Dubus et al. 1999), so they remain unilluminated, and do not produce the observed long decays. The best irradiated disc-instability models still use an *ad hoc* illumination parameter, such that the irradiation flux $F_{\text{irr}} = CL_X/(4\pi R^2)$ (Lasota 2001; Dubus et al. 2001). The reprocessed optical emission from this can fit broad-band optical/ultraviolet (UV) photometry of LMXBs (e.g. Gierliński, Done & Page 2009), but gives a slightly different dependence than predicted by Cunningham (1976), who approximates the disc as isothermal and derive the well-known scale height $H \propto R^{9/7}$ relation which leads to $F_{\text{irr}} \propto L_X/R^{12/7}$ (Hynes et al. 2002; Hynes 2005; Shidatsu, Done & Ueda 2016).

In addition, as is clear from the discussion above, the disc atmosphere is in no sense isothermal, and its scale height should vary as the illuminating spectrum changes. This effect can be very large as the outburst shows a dramatic spectral transition in a way which is now well studied (Fender, Belloni & Gallo 2004; Remillard & McClintock 2006). The spectrum starts off hard, dominated by Comptonization, typically peaking at 100 keV. It stays hard during the rapid rise, then abruptly softens, making a complex transition at high luminosity to a soft, disc-dominated state, typically peaking at $2(L/L_{\text{Edd}})^{1/4}$ keV (Done, Gierliński & Kubota 2007), before making a transition back to the hard state at around $L/L_{\text{Edd}} \sim 0.02$ (Maccarone 2003). Since this changing spectrum gives a very different heating/cooling balance, the wind/atmosphere responds by changing its density/scale height/launch radius (Done et al. 2018). This predicts the strength of illumination should change during the outburst, especially at the spectral transition.

We address the extent of these complexities produced by X-ray irradiation via modelling the changing multiwavelength spectra seen in a normal black hole binary outburst. We use the recently developed self-consistent model (energy conserving) covering a wide energy range from hard X-ray to infrared (IR) regime (Shidatsu et al. 2016). Our study enables us for the first time to find significant time variations in reprocessed fraction during outburst, to calculate how the X-ray scattered fraction should change, and to compare the observations and the predictions of reprocessing from scattering in the corona/wind. This is important for considering input values into the irradiated disc codes in order to predict the effect of X-ray illumination from a physical rather than phenomenological model, and for examining existing theories of disc instability including the effect of irradiation (Tetarenko et al. 2018). Thus, our investigations open the way to a better understanding of the role of X-ray irradiation in the time-varying broad-band spectra and light curves of LMXBs.

The amount of irradiation in the existing theories can only be well constrained with simultaneous multiwavelength optical/UV and X-ray data. In this study, we use the unique coverage obtained from five simultaneous *Hubble Space Telescope* (*HST*) and *Ross X-Ray Timing Explorer* (*RXTE*) spectra of the low galactic column black hole binary XTE J1859 + 226 during its 1999–2000 outburst (Hynes et al. 2002). Although previous works used photometric optical/UV data (e.g. Gierliński et al. 2009), spectroscopic data gives a much better determination of the continuum shape, which requires *HST* in order to get the spectrum extending into the UV regime. There are very few binaries for which such data exist,

especially as these are often highly reddened due to their galactic plane location, and one of them is XTE J1859 + 226. This object is regarded as one of normal black hole LMXBs in terms of the overall X-ray spectral behaviour and light variations (e.g. Pei et al. 2017; Nandi et al. 2018). Its multiwavelength spectra spanning the brightest high/soft states of the outburst went through the disc-dominated state on the decline and finally approached the transition to the low/hard state. Thus, all these data sets should be dominated by irradiated disc emission, whereas dim low/hard states can have additional contributions from cyclo-synchrotron emission from the hot electrons (Veledina, Poutanen & Vurm 2011) and synchrotron emission from the jet, which is more likely to be an IR component (Gandhi et al. 2011; Merloni, Di Matteo & Fabian 2000; Fender et al. 2004). These disc-dominated states are the simpler ones in which to explore the effect of reprocessing, and were fit to the optical/UV data by Hynes et al. (2002). However, these models were not able to simultaneously reproduce the X-ray spectra. Hence, there is no study explaining coherently the broad-band spectral characteristics, though there are multiple observations (Brocksopp et al. 2002; Zurita et al. 2002; Uemura et al. 2004; Casella et al. 2004; Farinelli et al. 2013; Sriram, Rao & Choi 2013).

The structure of this paper is the following. In Section 2, we display the overall X-ray and optical behaviour of the 1999–2000 outburst in XTE J1859 + 226, and in Section 3, we describe the data selection. In Section 4, the details of our model are given, and the results of broad-band spectral energy distributions (SED) analyses are shown in Sections 5 and 6. Finally, we interpret and discuss our results in Section 7, including the results of theoretical models, and summarize our conclusions in Section 8.

2 OVERALL X-RAY AND OPTICAL BEHAVIOUR

We use the *RXTE*/All-Sky Monitor (ASM) standard products to look at the overall evolution of the X-ray light curve during the outburst (see filled circles in the top panel of Fig. 1). The corresponding ASM hardness ratios, defined as 3–12 keV/1.5–3 keV (bands 2 + 3/band 1), are shown in the middle panel of Fig. 1. These show that the spectrum starts in the low/hard state (ASM hardness ratio around 2), then makes a transition to a softer state during the fast rise. Around the maximum, the X-ray brightness shows complex flaring (see also Brocksopp et al. 2002), and afterwards, it drops with an exponential decay with correlated spectral softening, interrupted by a plateau during MJD 51520–51545.

The *HST* data were taken on 1999 October 18, 1999 October 27, 1999 November 6, 2000 February 8, and 2000 March 5, which correspond to MJD 51469, 51478, 51488, 51582, and 51608, respectively. These times are indicated in Fig. 1 with vertical solid lines. Hereafter these are referred to as T1, T2, T3, T4, and T5. The UV and optical spectra of *HST* were taken by the Space Telescope Imaging Spectrograph, and reduced by the standard pipeline. The gratings used were G140L and G230L on the far-UV Multi-Anode Micro-channel Array (MAMA) detector, and G430L and G750L on the optical CCD. We put these in contexts of the optical evolution in the outburst by extracting the *R*-band data from fig. 2 in Zurita et al. (2002) (quadrangular points in the upper panel of Fig. 1). These show a smooth decline from T1 to T5.

The *RXTE*/Proportional Counter Array (PCA) pointed observations give much better spectra than the ASM, but they do not give continuous coverage of the outburst. We extract the 3–25 keV standard product spectra, and fit these in XSPEC with a model consisting of TBABS*(DISKBB + NTHCOMP) or

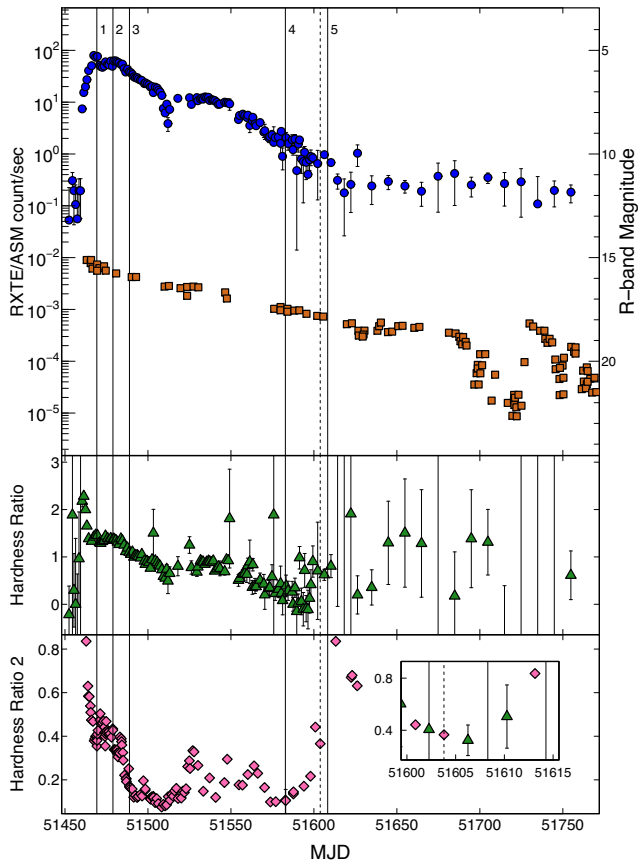


Figure 1. Overall X-ray light curve in the 1.5–12 keV band obtained by *RXTE*/ASM (circles) and overall optical *R*-band light curve digitized from fig. 2 in Zurita et al. (2002) (squares) during the 1999–2000 outburst in XTE J1859 + 226 (top panel), hardness ratio defined as 3–12 keV/1.5–3 keV in the *RXTE*/ASM data (middle panel), and hardness ratio calculated defined as 6–10 keV/3–6 keV in the *RXTE*/PCA data (bottom panel). The vertical solid lines labelled by 1, 2, 3, 4, and 5 represent MJD 51469, 51478, 51488, 51582, and 51608, respectively. The vertical dashed line shows February 29 in 2000 (MJD 51603). The data during MJD 51600–51680 are binned every 4 d, and those after MJD 51680 are binned every 10 d. The small window in the bottom panel shows an enlarged view of the hardness ratios during MJD 51600–51615. Here, -0.3 is added to the hardness ratios of *RXTE*/ASM data.

TBABS*SMEDGE*(DISKBB+NTHCOMP + GAUSSIAN), with hydrogen column fixed at $5.0 \times 10^{21} \text{ cm}^{-2}$. In this paper, we use XSPEC of HEASOFT version 6.23. We use these models to calculate the intrinsic hardness ratio (unabsorbed flux in 6–10/3–6 keV), shown in the bottom panel of Fig. 1. This shows that there are quasi-simultaneous *RXTE*/PCA data for T1–4, but that T5 occurs during a gap in the PCA data coverage. Importantly, this gap encompasses a state change in the X-ray spectrum. The nearest PCA data taken before the *HST* spectrum is in the soft state (PCA hardness ratio ~ 0.4), while the one after is in the hard state (PCA hardness ratio ~ 0.8). The inset in the bottom panel of Fig. 1 shows a zoom of this time period, with both the ASM hardness ratio (triangles, with -0.3 added to make them comparable) and the PCA hardness ratio (diamonds).

Fig. 2 shows the outburst evolution from the *RXTE*/PCA X-ray data on a hardness-intensity diagram, where we plot the unabsorbed hardness ratios from 6–10/3–6 keV, together with the unabsorbed 0.01–100 keV bolometric flux determined from the modelling. This

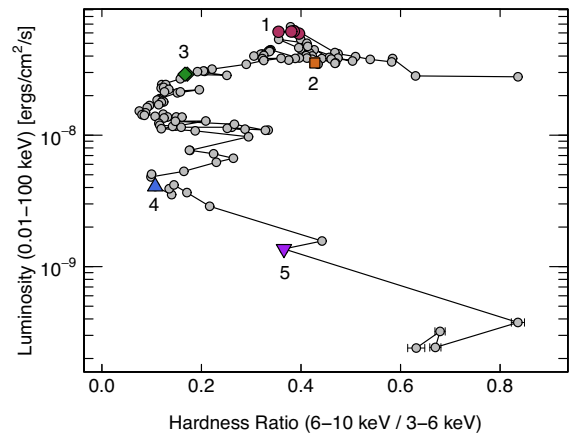


Figure 2. Hardness–intensity diagram during the 1999–2000 outburst in XTE J1859 + 226. The filled circles, square, diamonds, triangle, and inverted triangle represent the data on MJD 51469, 51478, 51488, 51582, and 51603, respectively.

reinforces the conclusions from the light curve and hardness ratios, that the source was in the very high state during T1–2 (red circle/orange square), then was in a bright soft state in T3 (green diamond), and a much dimmer soft state in T4 (blue triangle), while T5 (purple inverted triangle) was just before the transition back to the hard state.

3 SELECTION OF MULTIWAVELENGTH SPECTRAL DATA

Our focus is to model the continuum emission over as broad a bandpass as possible. We extract the *HST* data from the Mikulski Archive for Space Telescopes archive¹, removing any significant emission lines originating from the accretion disc (C IV (1550), He II (1640), He II (4686), H β , H α lines), as well as interstellar absorption lines (Si II, O I/Si II, C II, Ni III, Fe II, Fe II/Mn II, Mg II, and Mg I lines), and the geocoronal Ly α line. We bin the remaining points to obtain better signal-to-noise ratio. We then add 4 per cent and 5 per cent systematic errors to the MAMA data and the CCD data of *HST* spectra, respectively, considering the photometric accuracies.

We use the *RXTE* pipeline spectral products for the same dates corresponding to the *HST* data except for T5. As for T5, we instead use the nearest PCA data taken 5 d before the *HST* spectrum, considering the discussion in the preceding section. Also, we add 1 per cent systematic errors to the spectral data between 3–25 or 3–15 keV for the lower signal-to-noise spectra T4–5.

We extend the wavelength coverage down to the IR regime by using simultaneous photometric points taken by the United Kingdom Infrared Telescope 3.8-m telescope (Hynes et al. 2002). These are available for T1 (*K* band only), while T2 and T5 have *J*, *H*, and *K* bands.

¹Based on observations made with the NASA/ESA Hubble Space Telescope, obtained from the data archive at the Space Telescope Science Institute. STScI is operated by the Association of Universities for Research in Astronomy, Inc. under NASA contract NAS 5-26555.

4 MULTIWAVELENGTH SPECTRAL MODEL: OPTXRPLIR

Fitting the optical/UV together with the X-ray spectral data from an accretion flow is not straightforward. There is an evolving series of broad-band continuum SED models in the literature (Gierliński et al. 2009; Sutton, Done & Roberts 2014; Shidatsu et al. 2016). We describe here the most recent version (the OPTXRPLIR model: Shidatsu et al. 2016) for completeness. Its relation to earlier models is discussed in Shidatsu et al. (2016).

The strength of irradiation of the outer parts of the accretion disc by the inner flow depends on the intrinsic illumination pattern of the X-ray source, the shape of the outer disc, and its albedo. The shape of the outer disc is itself dependent on the X-ray illumination, with Cunningham (1976) showing that this results in $H(R) \propto R^{9/7}$ so that $T_{\text{irr}}(R) \propto R^{-3/7}$, contrasting with the standard unilluminated disc where $H(R) \propto R^{9/8}$ and $T_{\text{visc}}(R) \propto R^{-3/4}$. Hynes et al. (2002) use these relations to make a simple irradiated disc model, where $T_{\text{eff}}^4(R) = T_{\text{visc}}^4(R) + T_{\text{irr}}^4(R)$. This is able to fit the optical/UV spectra, but does not match the simultaneous X-ray data (see fig. 5 of Hynes et al. 2002). There are several reasons for this, firstly the model only incorporates the disc emission, although black hole binaries also show a power law which extends to significantly higher energies than expected for an optically thick disc. We assume that all the emission is powered by the standard Novikov–Thorne disc emissivity, and hence, the luminosity of the X-ray tail defines a radius, R_{pl} , below which the gravitational power released by accretion, must be dissipated in optically thin material leading to Comptonization, which is characterized by an electron temperature kT_{pl} and power-law spectral index Γ_{pl} , rather than making the highest temperature disc emission. The very high and intermediate states in black hole binaries have additional lower temperature Comptonization (e.g. Kubota & Done 2004), and hence, we similarly assume that this is powered by the luminosity released between R_{cor} and R_{pl} , which is characterized by an optical depth, τ and electron temperature kT_{warm} .

In addition, even where the high-energy X-ray emission is low, containing less than 10 per cent of the total emission, there is an offset in normalization between the optical/UV emission from the outer disc and the X-ray emission from the inner disc (see e.g. the upper panel of fig. 5 in Hynes et al. 2002). This mismatch is due instead to the different temperature and density of the X-ray emitting inner disc compared to the optical emitting outer disc. The true absorption opacity can be much smaller than the electron scattering opacity, leading to a modified rather than true blackbody spectrum (Shakura & Sunyaev 1973; Czerny & Elvis 1987). This emission can be approximated as a colour-temperature corrected blackbody, $B_{\nu}(f_{\text{col}}T_{\text{visc}})/f_{\text{col}}^4$, where f_{col} is a colour temperature correction factor which is ~ 1.6 – 2.6 at X-ray temperature but is ~ 1 at optical temperature (Shimura & Takahara 1995; Kubota, Makishima & Ebisawa 2001; Davis & Hubeny 2006; Done et al. 2012; Shidatsu et al. 2016). We use the analytic approximation to $f_{\text{col}}(T_{\text{visc}})$ calculated in the appendix of Davis & Hubeny (2006) as implemented in Done et al. (2012) for each annulus with $R > R_{\text{cor}}$. The lower line in the left-hand panel of Fig. 3 shows the resulting spectrum without irradiation and with only a fairly weak, hot corona ($R_{\text{cor}} = R_{\text{pl}} = 10R_{\text{g}}$) for $\log(L/L_{\text{Edd}}) = -1$. The hot Comptonization region has $\Gamma_{\text{pl}} = 2.0$ and $kT_{\text{pl}} = 100$ keV, while the disc is assumed to extend to an outer radius $R_{\text{out}} = 10^5 R_{\text{g}}$. The break in shape of the disc emission between the optical and X-ray components is clearly evident.

We incorporate irradiation by assuming about the disc height that $H(R)/R = f_{\text{out}}(R/R_{\text{out}})^{2/7}$, where f_{out} sets the fraction of luminosity

from the innermost radii which is intercepted by the outer disc. This is left as a free parameter rather than fixed to the self-consistent value in Cunningham (1976) to allow for additional effects such as scattering from a wind and/or limb darkening/brightening of the inner disc emission. The outer disc has some albedo a_{out} , so that only a fraction $(1 - a_{\text{out}})$ of the incident flux thermalizes. We set $a_{\text{out}} = 0.9$ on the assumption that the skin of the outer disc is highly ionized by the X-ray illumination (van Paradijs & McClintock 1994; Jimenez-Garate, Raymond & Liedahl 2002). The left-hand panel in Fig. 3 shows the change in optical/UV emission in increasing f_{out} from zero (the intrinsic emission from the accretion flow, dotted line) to weak irradiation with $f_{\text{out}} = 4 \times 10^{-3}$ (dashed line) to stronger irradiation with $f_{\text{out}} = 4 \times 10^{-2}$ (solid line).

In addition, irradiation also depends on luminosity and disc size. The middle panel in Fig. 3 shows the expected change as a function of increasing L/L_{Edd} for fixed $f_{\text{out}} = 4 \times 10^{-2}$. The optical reprocessed luminosity is $f_{\text{out}}L$, and emerges as a blackbody from the fixed size outer disc, so the monochromatic flux in the IR/optical regime on the Rayleigh–Jeans tail varies only as $\propto L^{1/4}$. This contrasts with the flux at UV and higher energies which changes by a much larger factor. The right-hand panel of Fig. 3 shows instead the effect of changing the size scale of the outer disc for fixed luminosity and reprocessed fraction. This changes the Rayleigh–Jeans IR/optical tail, with almost no effect on the emission at higher energies. Thus, the UV flux is most sensitive to the reprocessed fraction, the UV and X-ray emission together is most sensitive to the intrinsic luminosity, while the IR/optical emission is most sensitive to the size of the outer disc.

5 CONSTRAINING PARAMETERS IN BROAD-BAND FITTING WITH OPTXRPLIR

The model OPTXRPLIR contains the black hole mass and the distance to the object as free parameters. We constrain the range of the black hole mass to 6.16 – $15.5 M_{\odot}$ (Corral-Santana et al. 2011) and fix the distance of 8 kpc (Hynes 2005; Tetarenko et al. 2016). The black hole spin parameter a_* is fixed to 0. This model assumes a 60° inclination in computing the disc spectrum. We fix the normalization to 1, since the inclination of this object is suggested to be close to 60° (Corral-Santana et al. 2011). At this inclination and spin, the Doppler boosting of the inner disc emission is almost completely offset by gravitational redshift, and hence, we do not impose any relativistic corrections. We also fix the temperature of the hot corona at 100 keV, which is much higher than the energy range of RXTE/PCA data.

The hard X-rays from the corona can directly illuminate the inner disc as well as the outer disc. Some fraction of these are scattered (reflected) by electrons in the disc, while the remainder is absorbed by bound-free transitions which can be followed by fluorescent line emission. They combine and produce a reflected spectrum which rises sharply from 1 to 10 keV as the absorption opacity decreases, but with a strong iron edge and emission line superimposed. This can be approximately modelled using a smeared edge (SMEDGE), with the cross-section index fixed at -2.67 . We also include a Gaussian line where required by the data. We model the companion star as a constant blackbody component (BBDYRAD). This is a late-type K star according to Corral-Santana et al. (2011), and with temperature of 3.2 – 3.6×10^4 keV and radius of 4.5 – 6.2×10^5 km (Allen 1973).

To fit the raw data requires that we include reddening and absorption from dust and gas in the interstellar medium (ISM). We use the PHABS model for the gas phase as it does not include the

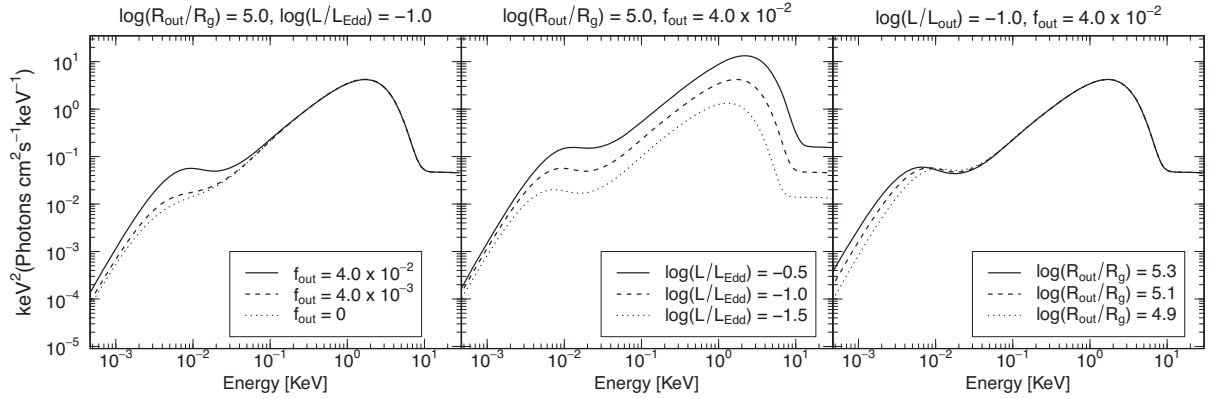


Figure 3. Model emission of the irradiated disc in the OPTXRPLIR model as a function of disc height (left-hand panel), or luminosity (middle panel), or outer disc radius (right-hand panel). Here, $r_{\text{cor}} = r_{\text{pl}}$, and the parameters r_{pl} and Γ are fixed to 8 and 2.0, respectively. The other fixed parameters are the same as those described in Section 4.1.

neutral edges below 13.6 eV (e.g. from Fe I). These are not present in our data at the expected level from neutral material due to the multiphase nature of the ISM, where most Fe is ionized to Fe II. We constrain N_{H} in the gas phase to the range $1.0\text{--}3.0 \times 10^{21} \text{ cm}^{-2}$ by using *ASCA*/GIS data on MJD 51474. This extends down below 1 keV and is more sensitive to absorption than the *RXTE*/*PCA* data.

There is a range of UV reddening curves even for a fixed $R_{\text{V}} = 3.1$ parameter which is the ratio of total to selective extinction at the optical *V* band (Fitzpatrick 1999; Cardelli, Clayton & Mathis 1989; Seaton 1979). These differ at the 20 percent level around the 2200 Å feature and at the shortest wavelengths (less than 1500 Å, see e.g. fig. 1 of Fitzpatrick 1999, or fig. 9 of Fitzpatrick & Massa 2007). Hynes (2005) used the reddening curve of Fitzpatrick (1999), but this is not available in XSPEC. Instead, we use the Seaton (1979) reddening model (UVRED in XSPEC) as being the closest to the Fitzpatrick (1999) curve around the 2200 Å feature. This only extends down to 3700 Å (3.4 eV), so we first fit all five datasets simultaneously, using a restricted energy range of 0.0034–25 keV with the model UVRED*PHABS*SMEDGE*(OPTXRPLIR), tying the extinction, column density and black hole mass across all datasets. We find best-fitting values for these of $E(B - V) = 0.526$, $N_{\text{H}} = 3.0 \times 10^{21} \text{ cm}^{-2}$, and mass of $6.9 M_{\odot}$. The best-fitting value of reddening is slightly different to the value of $E(B - V) = 0.58 \pm 0.12$ derived by Hynes et al. (2002), but this is due to the difference in shape of the reddening curve Fitzpatrick (1999). The effect of our reddening correction with $E(B - V) = 0.526$ from Seaton (1979) is very similar to that of $E(B - V) = 0.58$ from Fitzpatrick (1999). We use the extinction law from Cardelli et al. (1989) to extend the reddening down to the optical, having checked that the difference is within a few percents between Seaton (1979) and Cardelli et al. (1989) in the region above 3700 Å (Fitzpatrick & Massa 2007).

We then deredden the optical/UV/IR spectra with the best-fitting value of $E(B - V)$, and fit all five spectra simultaneously across the entire band with the model PHABS*SMEDGE*(BBODYRAD + OPTXRPLIR), to obtain the best-fitting values for the parameters of the companion star. The best-fitting temperature and radius are estimated to be $3.6 \times 10^{-4} \text{ keV}$ and $6.2 \times 10^5 \text{ km}$, respectively.

We note that the black hole mass, as well as being consistent with previous determinations, gives the luminosity just before the soft-to-hard transition of around 1–2 per cent of the Eddington luminosity, as expected from the advection-dominated accretion flow models of the low/hard state (Narayan & Yi 1995), and in line with what is generally observed (Maccarone 2003).

6 EVOLUTION OF THE ACCRETION FLOW

In this section, we fit the spectra at each epoch (T1–5) individually, using the deredden optical/UV data together with the *RXTE*/*PCA* X-ray data. We again fit with the model PHABS*SMEDGE*(BBODYRAD + OPTXRPLIR), but now have all the system parameters at their best-fitting values as determined in the preceding section in order to better constrain the remaining parameters of the accretion flow. We give the deconvolved, de-absorbed SED in the top window in Fig. 4, and show residuals to the best-fitting model in the small window below each spectrum. The best-fitting parameters and their errors are given in Table 1.

6.1 Modelling of the very high state at the early stage

The hardness-intensity diagram (see Fig. 2) clearly shows that the X-ray spectra in T1 and T2 are in the very high state. This state can show strong low-temperature and optically thick thermal Comptonization as well as a power-law tail to higher energies indicating a hotter, optically thin component (e.g. Życki, Done & Smith 2001; Kubota et al. 2001; Kubota & Done 2004). We deal with this component by allowing R_{cor} to be a separate free parameter, along with the electron temperature and optical depth of this component.

The initial fit of this baseline model to T1 and T2 shows an excellent match to the optical/X-ray spectra, but with a strong IR excess. This is most clearly seen in the residuals as for T2, which are displayed in the middle window of the upper right panel of Fig. 4, where there are IR data across *J*, *H*, and *K* bands. This could indicate a contribution from the radio jet. This is known to closely follow the hard X-ray Comptonized flux, even into the soft states (Zdziarski et al. 2011). The very high and intermediate states are often the ones with the strongest jet emission (Fender et al. 2004), and radio monitoring of XTE J1859 + 226 during this outburst showed that the radio luminosity was largest in these initial stages of the outburst (Brocksopp et al. 2002). We thus add a power law to approximately model the synchrotron jet emission. This gives a much better fit to the IR region, without changing the fit at higher energies (see the lower windows of the upper two panels in Fig. 4). By comparing the middle and bottom panels in the upper two panels of Fig. 4, we can see a significant jet contribution to the IR flux, with a rather steep synchrotron emission index of ~ 2.5 , which is consistent with the IR jet emission seen in GX 339 – 4, another black hole LMXB (Gandhi et al. 2011). As for the IR excess in T2, the contribution of

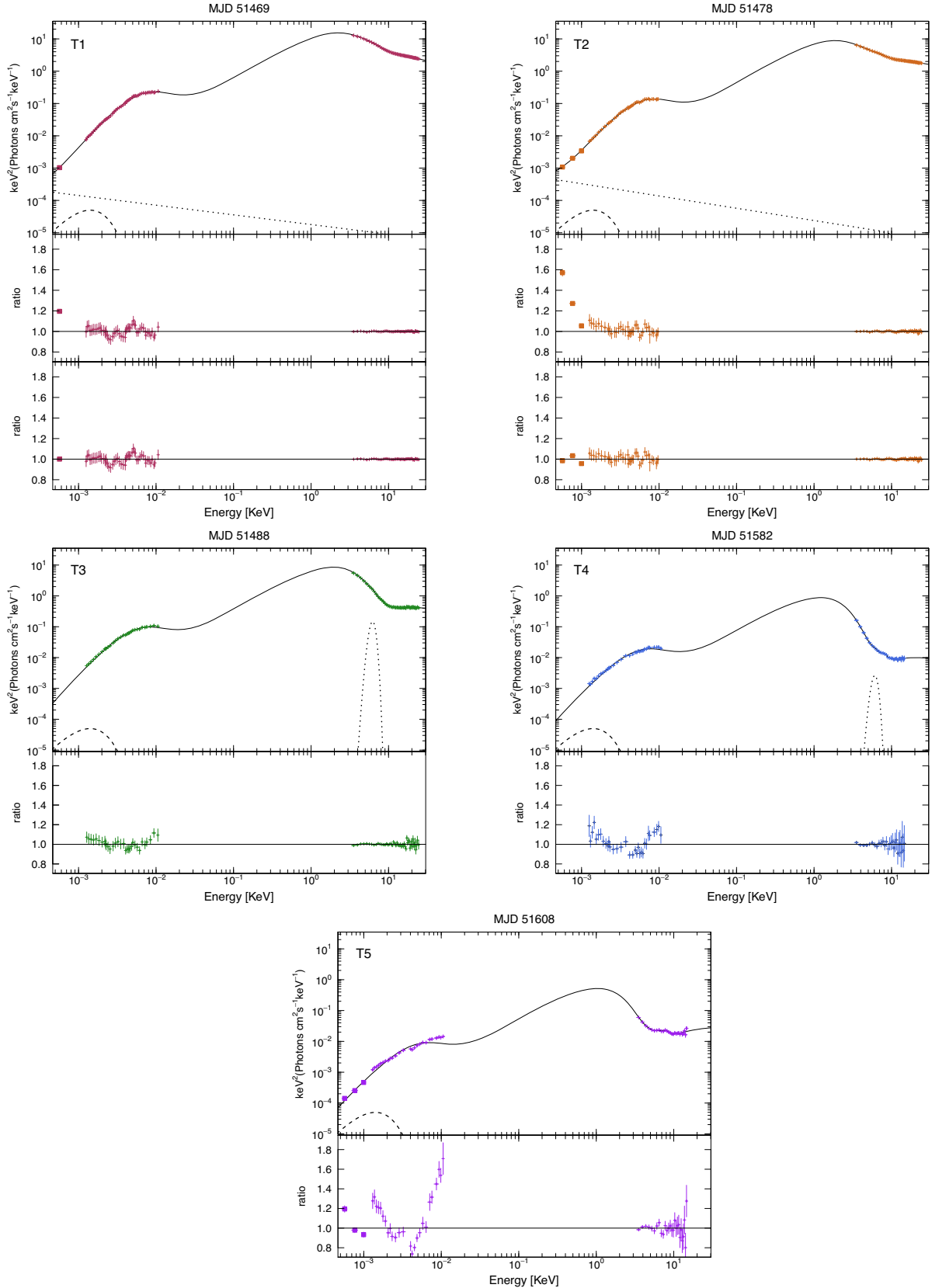


Figure 4. Multiwavelength SEDs and their ratios on T1–T5. On T1 and T2, we prepare the ratio without a power-law model for comparison in the middle windows. The crosses and solid line represent the observed SED and the emission reproduced by our model, respectively. The rectangles are the IR data. The dashed line represents the emission from the companion star. The dot line in the upper panels represents the model emission from synchrotron jet ejection, and that in the middle panels represents the model emission from iron line.

Table 1. Best-fitting parameters of our modelling in the five sets of broad-band spectra.

Model	Parameter	T1	T2	T3	T4	T5
smedge	E_c^*	7.6 ± 1.1	7.4 ± 1.0	8.4 ± 0.3	8.3 ± 1.7	8.1 ± 0.6
	f^\dagger	0.29 ± 0.71	0.5 ± 0.5	1.0 ± 0.3	1.0 ± 0.7	1.0 ± 0.6
	W^\ddagger	4.7 ± 34	5.6 ± 11.3	4.5 ± 1.4	2.3 ± 1.2	2.7 ± 2.2
Gaussian	E_1^\S	–	–	6.1 ± 0.3	6.0 ± 0.4	–
	σ^\P	–	–	0.50 ± 0.06	0.5 ± 0.5	–
	N_1^\lrcorner	–	–	$(4.9 \pm 1.5) \times 10^{-3}$	$(0.9 \pm 6.0) \times 10^{-5}$	–
pegpwlw	α^{**}	2.3 ± 2.8	2.4 ± 0.6	–	–	–
	$N_2^{\dagger\dagger}$	0.65 ± 0.53	1.4 ± 0.7	–	–	–
optxrplir	$\log(LL_{\text{Edd}})^{\ddagger\ddagger}$	-0.38 ± 0.09	-0.59 ± 0.02	-0.68 ± 0.01	-1.67 ± 0.01	-1.88 ± 0.02
	$R_{\text{cor}}^{\S\S}$	32 ± 50	22 ± 300	–	–	–
	$\log(R_{\text{out}}/R_g)^{\P\P}$	5.26 ± 0.01	5.23 ± 0.02	5.20 ± 0.01	4.92 ± 0.02	4.91 ± 0.01
	kT_{es}^\lrcorner	1.06 ± 0.16	1.1 ± 0.4	–	–	–
	τ^{***}	$\gtrsim 7.3$	$\gtrsim 4.7$	–	–	–
	$R_{\text{pl}}^{\dagger\dagger\dagger}$	19 ± 9	19 ± 1	10.30 ± 0.06	8.22 ± 0.25	10.81 ± 0.57
	$\Gamma^{\ddagger\ddagger\ddagger}$	2.42 ± 0.07	2.30 ± 0.06	2.17 ± 0.04	2.16 ± 0.24	1.83 ± 0.13
	$f_{\text{out}}^{\S\S\S}$	$(4.4 \pm 0.8) \times 10^{-2}$	$(4.0 \pm 0.3) \times 10^{-2}$	$(3.2 \pm 0.1) \times 10^{-2}$	$(6.2 \pm 0.3) \times 10^{-2}$	$(4.0 \pm 0.4) \times 10^{-2}$
	χ^2/dof	0.47	0.63	0.99	2.26	10.47

Notes: *Threshold energy of reflection in units of keV.

\dagger Maximum absorption factor at the threshold energy.

\ddagger Smearing width in units of keV.

\S Line energy in unit of keV.

\P Line width in unit of keV.

\lrcorner Total photons $\text{cm}^{-2} \text{s}^{-1}$ in the line of sight.

** Photon index of power law α .

$\dagger\dagger$ Flux in units of $10^{-12} \text{ erg cm}^{-2} \text{ s}^{-1}$ over the energy range (0.0005–0.02 keV).

$\ddagger\ddagger$ Luminosity divided by the Eddington luminosity in logarithmic scales.

$\S\S$ Radius of the low-temperature Comptonization component in units of R_g .

$\P\P$ Disc radius in units of R_g in logarithmic scales.

\lrcorner Temperature of the low-temperature Comptonization component in units of keV.

*** Optical depth in the low-temperature Comptonization component.

$\dagger\dagger\dagger$ Radius of the central hot corona in units of R_g .

$\ddagger\ddagger\ddagger$ Photon index of the central hot corona.

$\S\S\S$ Geometry-dependent factor of the thermalized fraction at the illuminated outer disc.

jet ejection is about 20 per cent, which is estimated from the model flux of the power-law component on XSPEC.

6.2 Modelling of the high/soft states

The X-ray spectra in T3 and T4 are clearly in the high/soft state according to the hardness–intensity diagram (see Fig. 2). Hence, we do not include the low-temperature Comptonization component that is considered in modelling of SEDs in the very high state in the previous subsection, i.e. we set $R_{\text{pl}} = R_{\text{cor}}$. We also now include a Gaussian line with upper limit on the width of 0.5 keV as there are small but significant residuals in the 6–7 keV bandpass which indicate that the phenomenological smedge model is not sufficient to describe the reflection spectrum from the inner disc in these data.

The best-fitting SEDs for T3 and T4 are shown in the middle panels in Fig. 4. The X-ray spectra are well reproduced by dominant disc emission, with a weak power-law Comptonized tail, and a small contribution from the iron line for both high/soft state SEDs. The UV and optical spectra for T3, taken only 10 d after the very high state and at similar luminosity, are well fitted by the expected irradiated disc emission. However, the optical/UV spectra of T4, taken about three months after T3 with order of magnitude lower luminosity, show small but significant deviations away from the irradiated disc

model, despite both the outer disc radius and height being free to vary. The best-fitting values of both these parameters are different from those of T1–3, with the disc outer radius being significantly smaller and the disc height being significantly larger. The fit is, however, quite poor, with χ^2/dof larger than 2, and thus, the error ranges on the parameters may not be reliable.

6.3 Modelling near the transition to the low/hard state

The spectrum T5 is the lowest luminosity spectrum, taken just before the transition back to the low/hard state (Fig. 2). This is adequately fit using only the smedge to model the reflection features, and does not require the separate Fe line emission. The resulting SED is represented in the bottom panel of Fig. 4, and we can see the multiwavelength fit is very poor.

Given that the X-rays are not strictly simultaneous in these data, and that the source was clearly in the low/hard state 4 d later, it is possible that the source was already in the low/hard state during the time of the T5 spectra. Thus, there could be a potential component from the jet as well as from an irradiated disc. However, the jet should contribute more in the IR emission, similar to T1–2, whereas the IR flux level is clearly fairly well matched by the data.

Instead, it is the UV flux which is most discrepant, being under-predicted by almost a factor 2 at the shortest wavelengths. This rules

out an origin in either the jet or from uncertainties in the K-type companion star luminosity or temperature as both of these are red components. This is because the R -band magnitude of the companion star must be dimmer than the minimum of $R = 23$ seen in the quiescent intervals in Fig. 1, which is 100 times fainter than the $R = 18$ seen during T5. Also, there is a small ~ 20 per cent discrepancy between the IR and reddest *HST* optical points but this could be due to time variability as these data are not strictly simultaneous. The small discontinuity between the red and blue *HST* spectra may be also due to variability.

The derived best-fitting values of disc outer radius and height are different from those of T1–3, with the disc outer radius being significantly smaller, similar to T4. However, the irradiated disc models now do not match well to the observed UV spectral curvature. The shape of the UV spectrum has hardened considerably (see the next section, and see the discussion of Hynes et al. 2002) and is now bluer than predicted by the irradiated disc models. Since this is a change in curvature, it cannot be produced by uncertainties in the absolute reddening curve, but instead is showing there is an intrinsic change in the shape of the UV spectrum.

6.4 Changing optical/UV spectral shape

We focus on the changing optical/UV spectral shape between the classic irradiated disc shape in T1–3 (described as UV soft spectra in Hynes et al. 2002) to the less curved shape of T4 and especially T5 (UV hard, Hynes et al. 2002). We look at this in a model independent way by computing the ratio of optical/UV data from the accretion flow in each epoch. We subtract the contribution of the companion star from each spectrum, and then estimate the ratios between the resultant fluxes. The ratio of T2/T1 is R12, the ratio of T3/T2 is R23 etc. These flux ratios are shown as a function of energy in Fig. 5. These show that R12 and R23 are slightly decreasing with increasing energy across the optical/UV band as expected for constant outer disc radius with slightly decreasing illuminating flux and bolometric luminosity (see also the left-hand and middle panels of Fig. 3).

The large drop in flux between T3 and T4 is evident in the much lower normalization of R34, but the flux ratio between these two widely separated epochs is unexpectedly fairly constant with energy. The model spectra shown in the middle panel of Fig. 3 show how the irradiated disc spectrum in the OPTXRPLIR model changes with changing only $\log(L/L_{\text{Edd}})$, and this clearly makes much more impact on the UV flux than on the optical flux. Instead, in the context of the irradiated disc models, to decrease the optical flux requires a smaller R_{out} (see also the right-hand panel of Fig. 3).

We explore whether a decrease in $\log(L/L_{\text{Edd}})$ and R_{out} can explain most of the observed change in optical/UV emission in T4. We fit the SED in T4 with f_{out} fixed to 4.0×10^{-2} similar to T1–3. While the resulting fit, shown in the left-hand panel of Fig. 6, has the same drop in $\log(L/L_{\text{Edd}})$ and $\log(R_{\text{out}}/R_g)$ as in the fit with a free f_{out} , this gives a better match to the optical data than the fit allowing f_{out} to be free (the right middle panel of Fig. 4), but a dramatically worse fit to the UV spectra (see the left-hand panel of Fig. 6). This mismatch is now similar to that of T5 in the previous section. The dashed–dotted line shows a comparison model where $\log(R_{\text{out}})$ is fixed at 5.2 as in T3, showing how the optical data strongly require a decrease in R_{out} to compensate for the change in $\log(L/L_{\text{Edd}})$. This strongly overpredicts the observed optical data.

All of these models assumed that the disc is in steady state, so that the intrinsic emission from the outer disc (which forms the lower limit to the optical flux) is from the same mass accretion rate as is required to power the observed simultaneous X-ray emission.

Instead, the *HST* data in T4 can be much better fitted by ignoring the simultaneous X-ray data, i.e. by assuming that the disc is not in steady state so that the mass accretion rate can vary with radius. The right-hand panel of Fig. 6 shows how the curvature across the entire optical/UV bandpass can be modelled by very weak illumination of a disc with an intrinsically higher mass accretion rate than that consistent with the X-ray emission. The curvature in the UV region is then almost entirely from the increasing colour temperature correction rather than from irradiation. The disc outer radius is again significantly smaller than in T1–3. The estimated parameters in these additional two SED fittings are given in Table 2. Thus, there is a potential solution to explain the shape of the *HST* spectrum in T4 if the outer disc is intrinsically hotter than expected from the mass accretion rate as measured from the inner disc.

The break in behaviour from T1–3 to T4 is even more marked in T5. The ratio R45 clearly has a strong energy dependence, with the UV flux changing by more than the optical flux (see the bottom panel of Fig. 5). We again show the effect of fixed $f_{\text{out}} = 4.0 \times 10^{-2}$, but this time with fixed $\log(R_{\text{out}}/R_g) = 5.0$ as seen in T4. This fits adequately (to within 20 per cent) to the optical and IR flux, but the UV excess becomes even larger than in the previous section (compare the bottom panel of Fig. 4 and the left-hand panel of Fig. 7). This is why the best-fitting irradiated disc model in the previous section had a larger f_{out} value.

The right-hand panel of Fig. 7 shows the result of fitting to the UV/optical/IR data without including the X-ray emission, i.e. allowing the disc to be non-steady state. We get a much better fit to the curvature in the optical/UV spectra by an unirradiated, but hotter intrinsic outer disc, with $\log(R_{\text{out}}/R_g) \sim 5.0$ as well as T4. Then, the best-fitting values of $\log(L/L_{\text{Edd}})$ and f_{out} are -1.09 and 1.1×10^{-8} , respectively. However, the fit here is never statistically acceptable unlike that in T4. The χ^2/dof is equal to 6.9, though the residuals are less than ~ 20 per cent, and could be potentially produced by variability between different wavelengths in the *HST* ranges. X-ray spectral changes are most rapid around the transition (see e.g. Dunn et al. 2010), which would mean that the reprocessed flux could also change rapidly. Nonetheless, the optical/UV spectra are better matched by the intrinsic disc emission than by reprocessed flux. If this is intrinsic flux, the level implies a mass accretion rate through the outer disc is ~ 5 times larger than that in the inner disc.

7 DISCUSSION

7.1 Time evolution of irradiation effect and disc size

The UV/optical/IR spectra on T1–3 are mainly explained by the canonical irradiation to a steady-state disc in our model (see also Sections 6.1 and 6.2), although the IR emission requires an additional component, probably from the jet, in T1 and T2. The amount of irradiation drops by 25 per cent as the source luminosity declines by a factor of 2 from T1 to T3. By contrast, our irradiation model fails to match the shape of the UV/optical spectra together with the X-ray spectra in the late stage of the outburst (T4–5, see also Sections 6.2–6.4). We first investigate theoretical ideas of how the irradiation should change, and then apply them to our data.

7.1.1 Theoretical models of irradiation

Here, we consider the structure of the irradiated disc to see if the observed f_{out} values can be matched by theoretical predictions. At first, we consider the irradiated disc model of Cunningham (1976).

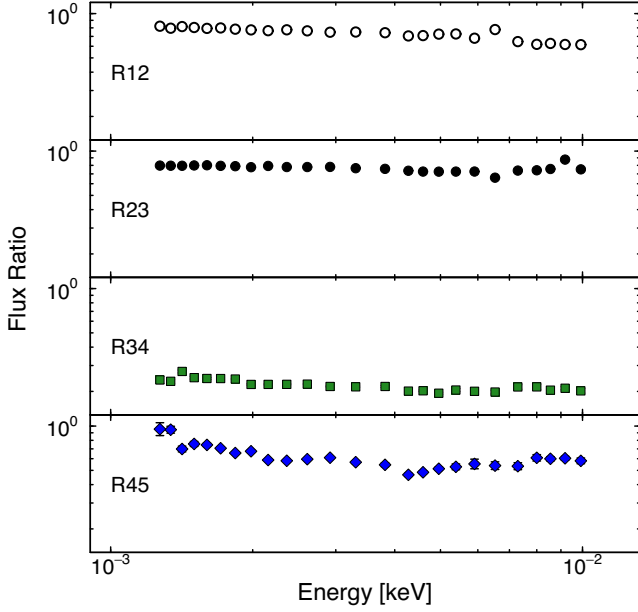


Figure 5. Flux ratio of the UV and optical spectra taken by *HST* between two adjacent time zones.

This has a prediction for the scale height of the outer disc when irradiation dominates. Recasting their equation (27c) into the units used here, gives

$$\begin{aligned} H/R &= 1.5 \times 10^{-3} (L/L_{\text{Edd}})^{1/7} (M_{\text{BH}}/M_{\odot})^{-1/7} \\ &\quad (R_{\text{out}}/R_{\text{g}})^{2/7} (R/R_{\text{out}})^{2/7} \\ &= f_{\text{d,out}} (R/R_{\text{out}})^{2/7}. \end{aligned}$$

This is derived by assuming 1/3 of the flux thermalizes in the disc, which is larger than the $(1 - a) = 0.1$ assumed here, but this will not affect predictions of changes in f_{out} .

Our source flux drops by a factor 2 from T1 to T3, so this equation predicts that this should cause a correlated decrease in f_{out} of around 10 per cent. This is very close to that observed. However, the absolute values of f_{out} underestimate that seen in the data by around a factor 2. We note that the larger thermalizing flux assumed in Cunningham (1976) will slightly underestimate f_{out} , so it suggests that there is an additional source of irradiation of the outer disc as well as direct illumination. Begelman et al. (1983) show that X-ray irradiation of the disc can result in a corona and wind. These features have some vertical scale height, so can scatter part of the central X-ray luminosity back down on to the outer disc. We briefly outline the theory of these X-ray heated winds and coronae, and then make a quantitative estimate of the additional irradiating flux produced by scattering in these structures.

Irradiation heats the disc surface to the Compton temperature, $kT_{\text{IC}} = \frac{1}{4} \int EL(E)dE / \int L(E)dE$, which depends only on the shape of the radiation field and not on its luminosity. This forms a corona above the disc with scale height set by the ratio of the sound speed $c_{\text{s,IC}}^2 = kT_{\text{IC}}/\mu$ (where μ is the mass) to the escape velocity $v_{\text{esc}}^2 \sim GM/R$. Wherever these are equal, the material can escape as a wind. This defines the wind launch radius as $R_{\text{IC}} = GM/c_{\text{IC}}^2$. At smaller radii, the material forms a static corona with scale height $H/R \sim c_{\text{s,IC}}/v_{\text{esc}} \sim (2R^3/R_{\text{IC}})^{1/2}$ (Begelman et al. 1983).

The wind region is a little more complex than the static corona as it is expanding so there is only finite time for heating. The heating rate depends on luminosity, so the detailed properties of the wind then depend on luminosity as well as spectral shape. This condition on the heating rate splits the wind region $R > R_{\text{IC}}$ into three separate zones (Begelman et al. 1983; Done et al. 2018). For $L > L_{\text{crit}}$, the wind is heated to T_{IC} so is launched at R_{IC} (isothermal free wind, region A). At larger radii, the heating rate decreases as the flux decreases, so eventually the wind is only heated to $T_{\text{ch}} < T_{\text{IC}}$. However, it still escapes as gravity is lower at these large radii (steadily heated wind, region B). Instead, if $L < L_{\text{crit}}$ then the material is heated only to $T_{\text{ch}} < T_{\text{IC}}$ at R_{IC} so it cannot escape (gravity inhibited, region C) but at larger radii, the escape speed for gravity decreases faster than the

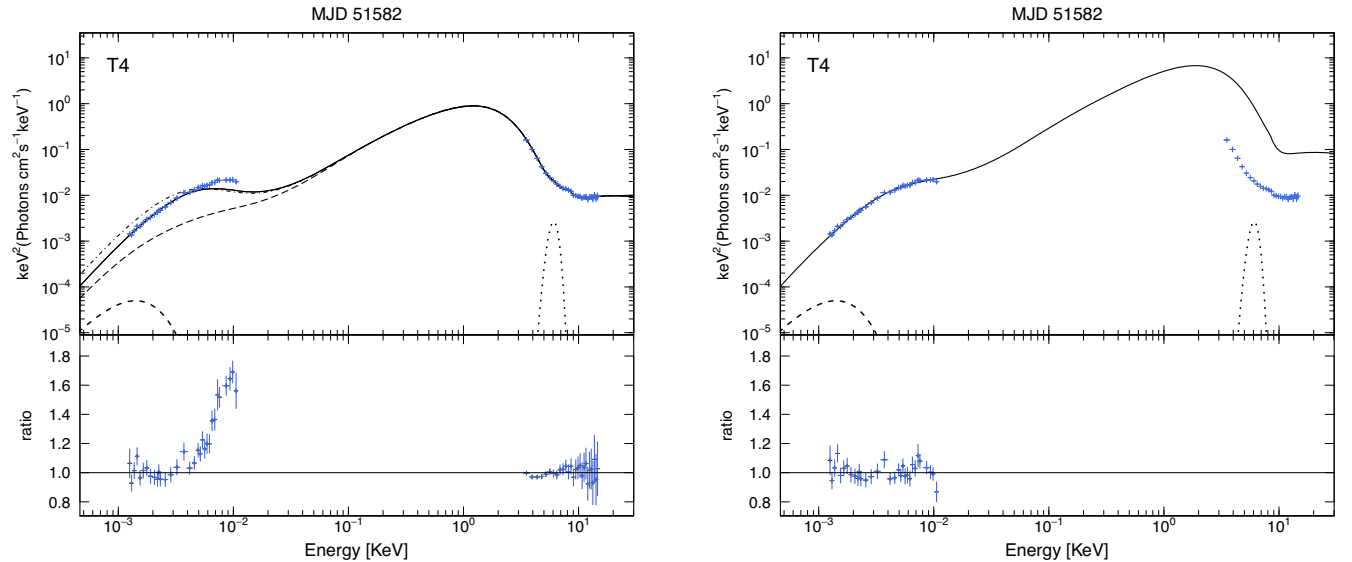


Figure 6. Multiwavelength SED modelling and the ratio of SED on T4 with f_{out} fixed to 4.0×10^{-2} (left-hand panel), and those without the X-ray spectra (right-hand panel). The crosses and solid line represent the observed SED and the emission reproduced by our model, respectively. The dashed and dot lines represent the emission from the companion star and that from iron line, respectively. The dash-dotted line in the left-hand panel is the model with $\log(R_{\text{out}}/R_{\text{g}}) = 5.2$. The long-dashed line in the left-hand panel represents an unirradiated disc.

Table 2. Best-fitting parameters of our additional SED modellings on T4. See the notations in Table 1 for the notation of each parameter.

Model	Parameter	T4 (f_{out} fix)	T4 (only <i>HST</i> spectra)
optxrplir	$\log(L/L_{\text{Edd}})$	-1.67	-0.80 ± 0.08
	$\log(R_{\text{out}}/R_{\text{g}})$	5.01 ± 0.01	5.00 ± 0.03
	f_{out}	4.0×10^{-2} (fix)	$(1.8 \pm 1.4) \times 10^{-3}$

decrease in characteristic temperature with flux so the wind can be launched (region B again).

Hence, the transition between the wind and atmosphere (i.e. wind launch radius) marks the boundary between region B and C, which is at $R \sim (L/L_{\text{crit}})^{-1}R_{\text{IC}}$ (with some dependence on Compton temperature, Woods et al. 1996; Higginbottom & Proga 2015; Done et al. 2018). A more careful treatment shows that the material escapes as a wind when $R_{\text{in}} > 0.2R_{\text{IC}}$ for $L > L_{\text{crit}}$, and when $R_{\text{in}} > 0.2(L/L_{\text{crit}})^{-1}R_{\text{IC}}$ for $L < L_{\text{crit}}$. Hence, there are only two regions where the material escapes efficiently as a wind, region A (where the wind is heated to T_{IC} as $L > L_{\text{crit}}$) and region B (where $T_{\text{ch}} < T_{\text{IC}}$ but $c_{\text{ch}} > v_{\text{esc}}$).

In the discussion above, the wind and corona are smoothly connected. However, the disc has fairly low scale height, so the direct illumination is always at grazing incidence. This means that optical depth effects can become important, where the inner corona becomes optically thick to grazing incidence paths, and casts a shadow. This suppresses corona formation by direct illumination until the shape of the disc photosphere itself rises above the shadow (Begelman & McKee 1983). Thus, the inner corona and outer corona/wind form separate structures. The inner corona does scatter some fraction of the central radiation, forming a diffuse source. However, this source is at small radii, where the scale height of the material is low due to the strong gravity, so this diffuse source is not much larger than the intrinsic source size so does not contribute to increasing the illumination of the outer disc.

On the other hand, scattering from the wind may form a larger scale height structure. The scattered flux from the wind forms a diffuse source of radiation which is maximized at the launch radius

R_{in} , where it has typical height $H_{\text{w}}(R_{\text{in}}) \approx R_{\text{in}}$. This forms an additional X-ray source which can efficiently illuminate the outer disc. Begelman & McKee (1983) show that the scattered luminosity is

$$\frac{L_{\text{sc}}(\text{wind})}{L} = \frac{L}{L_{\text{Edd}} \Xi_{\text{c,max}}} \begin{cases} 0.5 & (A) \\ \left(\frac{L_{\text{crit}}}{L}\right)^{2/3} [11 - 7(R_{\text{out}}/R_{\text{IC}})] & (B) \\ 9[1 + \ln(R_{\text{out}}/R_{\text{IC}})] & (C) \end{cases}$$

for wind regions A, B, and C, respectively (Begelman & McKee 1983, their equation 3.9), where $\Xi_{\text{c,max}} \approx 10$ is the maximum ionization parameter on the cold branch. We note that this approximation is not piecewise continuous, nor does it take into account the increase in the wind mass loss expected as the source approaches L_{Edd} due to the significant radiation pressure.

Thus, there are two components to the flux seen by the outer disc. One of them is direct illumination from the central source, which depends on the flaring of the disc and is $\propto H_{\text{d}}/R$, and the other is from scattering in the outer corona/wind $\propto L_{\text{sc}}(\text{wind})(H_{\text{w}}/R) \sim L_{\text{sc}}(\text{wind})$. Thus the total flux seen by the outer disc can be approximated as $L + L_{\text{sc}}(\text{wind})$ i.e. giving an effective $f_{\text{out}} \approx f_{\text{d, out}} + L_{\text{sc}}(\text{wind})/L$.

7.1.2 Application to XTE J1859 + 226

We evaluate T_{IC} from the spectral shape for T1–5, using a maximum energy of 100 keV for the flux integration to mimic the effect of the Klein–Nisina reduction in Compton scattering cross-section. We use this to derive L_{crit} and R_{IC} for all of our data sets. We tabulate the predicted thermal wind parameters in Table 3. There is a marked drop in T_{IC} linked to an increase in L_{crit} and R_{IC} as the source softens from the very high state at T1–2 to the bright high/soft state at T3, but all these bright spectra (T1–3) have $L > L_{\text{crit}}$, and hence have a wind region which starts at $R_{\text{in}} = 0.2R_{\text{IC}}$. Also, the wind region is A, since $R_{\text{out}} > R_{\text{IC}}$ at the outer disc radius. The ignition radius of the wind is just within the outer region of the disc in these data, but the expected mass-loss rate is fairly low as the outer disc radius is fairly small.

The values for f_{out} from combining the theoretical models of scale height of the irradiated outer disc and scattering from the wind are

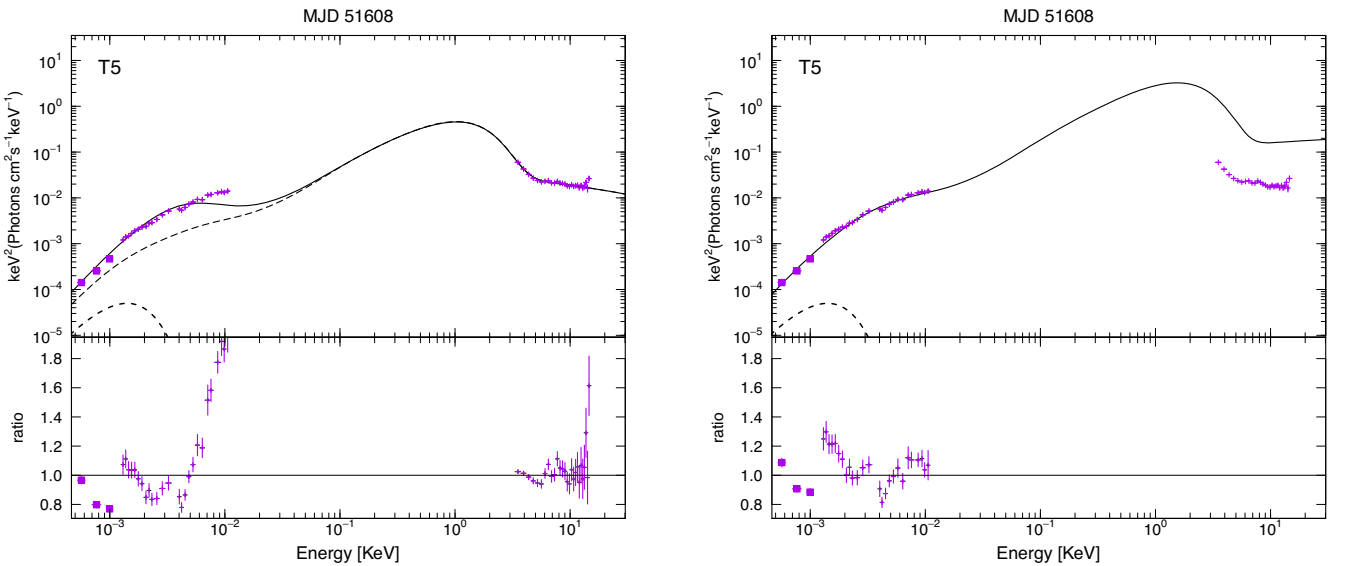


Figure 7. Multiwavelength SED modelling and the ratio of SED on T5 with fixed f_{out} and $\log(R_{\text{out}}/R_{\text{g}})$ (left-hand panel) and those without the X-ray data (right-hand panel). The crosses and solid line represent the observed SED and the emission reproduced by our model, respectively. The rectangles are the IR data. The dashed line represents the emission from the companion star. The long-dashed line in the left-hand panel represents an unirradiated disc.

Table 3. Thermal corona/wind parameters in T1–5. We use the luminosity and R_{out} summarized in Table 1 in these calculations.

Parameters	T1	T2	T3	T4	T5
T_{IC}^*	1.44	1.65	0.85	0.38	0.80
$R_{\text{in}}/R_{\text{g}}^\dagger$	8.0×10^4	7.0×10^4	1.3×10^5	No wind	No wind
$L_{\text{est}}/L_{\text{crit}}^\ddagger$	5.7	3.7	2.2	0.15	0.13
$\dot{M}_{\text{wind}}/\dot{M}_{\text{acc}}^\S$	0.29	0.31	0.09	–	–
$f_{\text{d,out}}^\P$	0.032	0.029	0.028	0.017	0.016
R_{ia}^\lrcorner	445	326	410	196	106
$H_{\text{c}}(R_{\text{ia}})^{**}$	21	14	15	3.2	1.9
$L_{\text{sc,wind}}/L_{\text{est}}^{\dagger\dagger}$	0.021	0.013	0.010	–	–
$f_{\text{out}}^{\ddagger\dagger}$	0.053	0.050	0.041	0.017	0.016

Notes: *Inverse-Compton temperature estimated from the spectral shape. In units of keV.

† Innermost radius where the wind is efficient.

‡ Ratio of the estimated luminosity against the critical luminosity, with which the wind can be triggered.

§ Ratio of the wind accretion against the whole accretion rate.

¶ Scale height of an outer disc defined by equation (27c) in Cunningham (1976).

$^\lrcorner$ Radius of an inner attenuation zone derived from equation (2.23) in Begelman & McKee (1983).

** Typical height of an inner attenuation zone derived from equation (2.6) and R_{ia} in Begelman & McKee (1983).

†† Scattered luminosity from a wind according to equation (3.9) in Begelman & McKee (1983).

‡† Predicted total f_{out} estimated by $f_{\text{d,out}} + L_{\text{sc,wind}}/L_{\text{est}}$.

remarkably close to those observed in T1–3. The absolute values are slightly dependent on the albedo assumed (see the discussion in Section 7.1.1), but the predicted changes in f_{out} should be more robust. Importantly, the models predict similar decrease in f_{out} as seen in the data as the source flux and T_{IC} drop from T1 to T3.

Conversely, T4 has a much lower luminosity. It is still disc dominated, but T_{IC} is low because of the cooler disc. Also, $R_{\text{in}} > R_{\text{out}}$ because $L < L_{\text{crit}}$. Thus there should be no wind region, only a static corona heated to T_{IC} . The disc scale height should be smaller intrinsically due to the lower luminosity, and there should be almost no additional scattered flux as there is very little wind. Yet the best fit to the data gives a much larger f_{out} , since it (poorly) fits the observational UV flux under the assumption of a steady-state disc, with the same mass accretion rate powering the intrinsic X-ray and optical/UV emission (see also Sections 6.2 and 6.4).

T5 has similarly low luminosity, though the X-ray tail is somewhat stronger (though quite poorly constrained), giving T_{IC} which is comparable to T3. However, the lower luminosity again means that $L < L_{\text{crit}}$. There is neither strong wind region nor additional source of illuminating flux to increase f_{out} . Thus, like T4, the models predict that $f_{\text{out,d}}$ is small due to the low luminosity, and $f_{\text{out}} \sim f_{\text{out,d}}$. Yet again the data require a much larger f_{out} than seen in T1–3 in order to (very poorly) fit the observational UV flux under the assumption of steady state in fitting broad-band data simultaneously (see also Sections 6.3 and 6.4).

Thus the irradiated disc theory, where the irradiation is a combination of direct illumination from the bright central regions, and its scattered flux from a wind, matches very well to the initial spectra in T1–3. However, these models predict that we should see a smaller reprocessed fraction in the dimmer spectra in T4–5, yet the data require a larger fraction to poorly (T4), or very poorly (T5) fit the data (see Sections 6.2–6.4). While T5 may be more complex due to its proximity to the spectral transition, and constraints from this spectrum are less secure due to the non-simultaneity of the X-ray data,

T4 is a classic disc-dominated state, and the X-ray and UV/optical data were simultaneously observed. Thus, T4 would show robustly that the irradiated steady-state disc models are broken. As proposed in Section 6.4, the intrinsic heating of the outer disc is possibly larger than expected for the same mass accretion rate as seen in the inner regions.

7.2 Time evolution of outer disc radius

Another key difference between T1–3 and T4–5 is that the disc outer radius has clearly decreased by ~ 15 per cent (see also Hynes et al. 2002). Some disc shrinkage is expected in the standard irradiated disc instability model (Dubus et al. 2001), but not as much as the factor 2 seen in these data. However, we can understand the degree of shrinkage by considering that disc extended much larger at the initial stage of the outburst than expected by the thermal instability. The thermal-tidal instability in low-mass ratio objects makes it possible (Ichikawa, Hirose & Osaki 1993).

The thermal instability triggers a mild increase in disc size, but if this crosses the radius at which it goes into 3:1 resonance with the binary orbit then the disc is unstable against a non-axisymmetric perturbation. This is a slowly growing mode, which forms an eccentric disc which precesses in the orbiting frame as its period is slightly longer than the orbit. This produces the superhump modulation seen in the optical light curves. The elliptical disc enhances the angular momentum transport with the companion star, which drives mass accretion through the outer disc, resulting in fast shrinkage of the disc. This combined thermal-tidal instability mechanism was first proposed for the SU UMa-type dwarf novae which typically have $q \lesssim 0.25$ and orbital periods of a few hours (Whitehurst 1988; Osaki 1989). Even more extreme mass ratio systems such as the WZ Sge-type dwarf novae, an extreme subclass of SU UMa-type dwarf novae, with $q \lesssim 0.08$, can trigger a tidal instability at the 2:1 resonance radius. The radius is larger than the 3:1 resonance radius, and this tidal instability grows faster. It forms spiral arms with period very close to the orbital period, and early superhumps are believed to be its representation (Osaki & Meyer 2002). Whichever tidal instability is triggered, the additional angular momentum transport and heating of the outer disc can keep it above the level of the hydrogen ionization instability, so can give long, exponential decline light curves even without X-ray irradiation (Osaki 1989).

XTE J1859+226 has an extremely small mass ratio, $q = M_2/M_{\text{BH}} \sim 0.09$, and its orbital period is 6.6 h (Corral-Santana et al. 2011). In this system, the disc radius will definitely exceed the 3:1 resonance radius, $\sim 0.47a$ in this object, so should trigger the thermal-tidal instability. Also, since the estimated disc radius in T1 exceeds the 2:1 resonance radius at $\sim 0.61a$ in this object, so we should see early superhumps with period almost equal to the orbital period at the early stage of its outbursts, and ordinary superhumps later in the outburst with period slightly longer than the orbit. Although there are no time-resolved optical light curves to unambiguously test this, Uemura et al. (2004) and Zurita et al. (2002) found some optical modulations with time-scale close to the orbital period, which they suggested to be superhump candidates. In addition, that outburst showed reflare according to Zurita et al. (2002), which are one of characteristic features in the outbursts of WZ Sge-type stars (Kato 2015).

7.3 Irregular disc geometry at the late outburst

On T4 and T5, we do not obtain reasonable fits, and the observations are inconsistent with the theoretical predictions as described

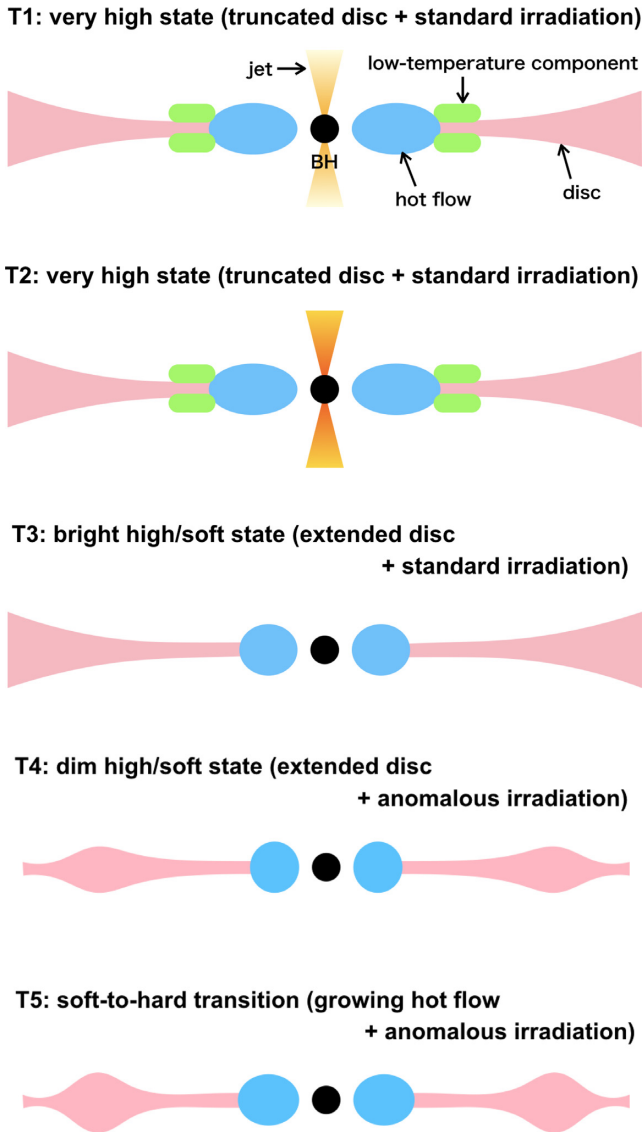


Figure 8. Schematic picture of time-evolved accretion geometry in the 1999–2000 outburst of XTE J1859 + 226. The black circle is a black hole. The pink, blue, green, and orange structures represent an accretion disc, an optically thin hot flow, a low-temperature optically thick Comptonization component, and jet ejection, respectively (colour online).

in Section 7.1.2. Considering that other emission mechanisms like jet ejections are unlikely, we suggest that the assumptions in our model are not applicable for T4 and T5, i.e. irregular outer disc geometry possibly producing non-steady state would be formed in this outburst. Here, we consider the thermal-tidal instability possibly forms an anomalous outer disc geometry. To date, the only calculations of the thermal-tidal instability in black hole binaries did not include the interplay of this with the X-ray irradiation heating (Ichikawa, Mineshige & Kato 1994), but they showed that the disc has a complex temperature dependence (see figs 3 and 5 in that paper). In addition, the tidal heating could increase the scale height of the outer disc, and/or changes its shape from the expected $H/R \propto R^{2/7}$ due to the piled-up mass at the outer disc (Osaki 1989). Thus, the effect can produce weird outer disc geometry related to non-steady state that we propose at T4–5 as sketched in Fig. 8, although the model in Ichikawa et al. (1994) predicts a rather complex

temperature dependence in the outer disc, whereas the spectra in T4 and T5 are best fit by the standard temperature distribution in the outer disc, with just an increased mass accretion rate relative to the inner disc. In the future, full calculations should include the effect of X-ray heating and see whether this in combination with the thermal-tidal instability can reproduce the observed data.

There are not many other possibilities which can explain the hot outer disc as seen in T4 and T5. Wind losses should also be included since these necessarily reduce the mass accretion rate between the inner and outer discs. However, the thermal wind is not strong in this system as the disc is small, and its effect should be biggest in T1–3, whereas the data most require a non-steady-state disc in T4–5. The effect of magnetic winds is difficult to quantify, but there may not be a strong requirement for these in the black hole binaries (Done et al. 2018). Hynes et al. (2002) suggest that the difference in optical/UV spectral shape arises from warping of the disc due to irradiation (Wijers & Pringle 1999; Ogilvie & Dubus 2001); however, this seems unlikely because this kind of instability is most effective in long-period (more than 1 d) systems. Full calculations are required in order to study the interplay of all these effects.

These possibilities raised above may be testable with fast photometric data simultaneous with X-ray observations. If the model in Ichikawa et al. (1994) is correct, the optical/UV emission is dominated by intrinsic luminosity of the underlying disc at the outer region, and hence, it will vary only very slowly, and non-correlated optical variability inherent to the outer disc may be observable. On the contrary, if the emission is dominated by reprocessing, the optical/UV variations will significantly correlate with the X-ray fast variations. If the warp precessions are dominant, strong optical periodicity as well as fast optical variability from reprocessing would be observed. If we solve this problem, we can know correctly the reason of the slow optical decline in outburst in LMXBs. Not only XTE J1859 + 226 but also many black hole X-ray binaries show more rapid X-ray outburst decay than the optical decay (Chen et al. 1997), so this is a common observational feature. X-ray irradiation is considered to form the slow decay of optical outburst light curves in LMXBs (Dubus et al. 2001); however, if the irradiation effect is weak at the late stage of outbursts, the tidal forces by the companion stars would be plausible. In many systems, it has not yet been constrained well which of the two is dominant.

8 CONCLUSIONS

We analysed the five sets of broad-band spectra from XTE J1859 + 226 during its 1999–2000 outburst by using the best current model of the irradiated disc continuum with the expected irradiation dominated $H \propto R^{9/7}$ shape, giving $T(R) \propto R^{-3/14}$. This works extremely well in the bright stages of the outburst, and is able to fit the X-ray, UV, and optical continua spectra, though the IR requires a small contribution from the jet whose power tracks the hard X-ray continuum. The solid angle subtended by the irradiated outer disc is observed to decrease by ~ 25 per cent as the source flux drops by a factor 2, and the spectrum softens from the very high state to the disc-dominated high soft state. The changing solid angle implied our fits are exactly consistent with the predictions of scale height of the irradiated outer disc and scattering in a thermal wind at the early stage of the outburst, with an albedo of ~ 0.9 .

The last two spectra, which are much lower in X-ray flux, are not well explained by these models. Since the optical and UV spectra have a different shape than predicted by the standard illuminated disc, it is difficult to precisely evaluate the amount of irradiation in these spectra. None the less, the straightforward model fits require

that a larger fraction of the flux is intercepted by the outer disc. However, the irradiated disc models predict the opposite: the scale height of the outer disc becomes smaller at these lower luminosities, and the thermal wind models predict that the wind should shut off at these low luminosities and temperatures. These late spectra are instead better fit by the unilluminated standard disc, which has $T \propto R^{-3/4}$. However, the models without illumination have an implied mass accretion rate through the outer disc, which is much higher than that which powers the inner disc. Our analyses also imply that the outer disc shrinks by more than a factor of 2.

The observed large shrinkage of the disc can be triggered by enhanced dissipation due to the thermal-tidal instability. Since this system likely has an extremely small mass ratio, this kind of instability should work. The tidal instability may also explain the different optical/UV spectra seen as the outburst dims as it produces additional heating of the outer disc and the resulting temperature distribution can be far from the steady state $R^{-3/4}$. However, there are no simulations to date of the thermal-tidal instability including the effects of X-ray illumination, so these models are not self-consistent. The tidal instability may also change the vertical structure of the outer disc in a non axisymmetric way, so that the disc geometry can be changed from that predicted by the irradiated disc models.

Better models including all these effects during the outburst may be able to match the observed behaviour, while better data – specifically including high time-resolution UV photometry such as UVSat (Pigulski et al. 2017) – should determine whether the UV flux in these dimmer spectra is due to X-ray irradiation or intrinsic heating of the outer disc.

ACKNOWLEDGEMENTS

This work was financially supported by the Grant-in-Aid for JSPS Fellows for young researchers (MK). CD acknowledges the Science and Technology Facilities Council through grant ST/P000541/1 for support.

REFERENCES

Allen C. W., 1973, *Astrophysical Quantities*, Athlone Press, London
 Begelman M. C., McKee C. F., 1983, *ApJ*, 271, 89
 Begelman M. C., McKee C. F., Shields G. A., 1983, *ApJ*, 271, 70
 Brocksopp C. et al., 2002, *MNRAS*, 331, 765
 Cardelli J. A., Clayton G. C., Mathis J. S., 1989, *ApJ*, 345, 245
 Casella P., Belloni T., Homan J., Stella L., 2004, *A&A*, 426, 587
 Chen W., Shrader C. R., Livio M., 1997, *ApJ*, 491, 312
 Coriat M., Fender R. P., Dubus G., 2012, *MNRAS*, 424, 1991
 Corral-Santana J. M., Casares J., Shahbaz T., Zurita C., Martínez-Pais I. G., Rodríguez-Gil P., 2011, *MNRAS*, 413, L15
 Cunningham C., 1976, *ApJ*, 208, 534
 Czerny B., Elvis M., 1987, *ApJ*, 321, 305
 Davis S. W., Hubeny I., 2006, *ApJS*, 164, 530
 de Jong J. A., van Paradijs J., Augusteyn T., 1996, *A&A*, 314, 484
 Done C., Gierliński M., Kubota A., 2007, *A&AR*, 15, 1
 Done C., Davis S. W., Jin C., Blaes O., Ward M., 2012, *MNRAS*, 420, 1848
 Done C., Tomaru R., Takahashi T., 2018, *MNRAS*, 473, 838
 Dubus G., Lasota J.-P., Hameury J.-M., Charles P., 1999, *MNRAS*, 303, 139
 Dubus G., Hameury J.-M., Lasota J.-P., 2001, *A&A*, 373, 251
 Dunn R. J. H., Fender R. P., Körding E. G., Belloni T., Cabanac C., 2010, *MNRAS*, 403, 61

Farinelli R. et al., 2013, *MNRAS*, 428, 3295
 Fender R. P., Belloni T. M., Gallo E., 2004, *MNRAS*, 355, 1105
 Fitzpatrick E. L., 1999, *PASP*, 111, 63
 Fitzpatrick E. L., Massa D., 2007, *ApJ*, 663, 320
 Gandhi P. et al., 2011, *ApJ*, 740, L13
 Gierliński M., Done C., Page K., 2009, *MNRAS*, 392, 1106
 Higginbottom N., Proga D., 2015, *ApJ*, 807, 107
 Hynes R. I., 2005, *ApJ*, 623, 1026
 Hynes R. I., Haswell C. A., Chaty S., Shrader C. R., Cui W., 2002, *MNRAS*, 331, 169
 Ichikawa S., Hirose M., Osaki Y., 1993, *PASJ*, 45, 243
 Ichikawa S., Mineshige S., Kato T., 1994, *ApJ*, 435, 748
 Jimenez-Garate M. A., Raymond J. C., Liedahl D. A., 2002, *ApJ*, 581, 1297
 Kato T., 2015, *PASJ*, 67, 108
 King A. R., 1998, *MNRAS*, 296, L42
 King A. R., Ritter H., 1998, *MNRAS*, 293, 42P
 Krolik J. H., Kallman T. R., 1982, *BAAS*, 14, 955
 Kubota A., Done C., 2004, *MNRAS*, 353, 980
 Kubota A., Makishima K., Ebisawa K., 2001, *ApJ*, 560, L147
 Lasota J.-P., 2001, *New Astron. Rev.*, 45, 449
 Maccarone T. J., 2003, *A&A*, 409, 697
 Merloni A., Di Matteo T., Fabian A. C., 2000, *MNRAS*, 318, L15
 Mineshige S., Wheeler J. C., 1989, *ApJ*, 343, 241
 Nandi A. et al., 2018, *Ap&SS*, 363, 90
 Narayan R., Yi I., 1995, *ApJ*, 452, 710
 Ogilvie G. I., Dubus G., 2001, *MNRAS*, 320, 485
 Osaki Y., 1989, *PASJ*, 41, 1005
 Osaki Y., 1996, *PASP*, 108, 39
 Osaki Y., Meyer F., 2002, *A&A*, 383, 574
 Pei S., Ding G., Li Z., Lei Y., Yuen R., Qu J., 2017, *Ap&SS*, 362, 118
 Pigulski A. et al., 2017, in Zwintz K., Poretti E., eds, *Second BRITe-Constellation Science Conference: Small Satellites, Big Science*, Proceedings of the Polish Astronomical Society, Vol. 5, held 22-26 August, 2016 in Innsbruck, Austria, Polish Astronomical Society which is located at Bartycka 18, 00-716 Warsaw, Poland, p. 76
 Remillard R. A., McClintock J. E., 2006, *ARA&A*, 44, 49
 Seaton M. J., 1979, *MNRAS*, 187, 73P
 Shakura N. I., Sunyaev R. A., 1973, *A&A*, 24, 337
 Shidatsu M., Done C., Ueda Y., 2016, *ApJ*, 823, 159
 Shimura T., Takahara F., 1995, *ApJ*, 445, 780
 Sriram K., Rao A. R., Choi C. S., 2013, *ApJ*, 775, 28
 Sutton A. D., Done C., Roberts T. P., 2014, *MNRAS*, 444, 2415
 Tanaka Y., Shibazaki N., 1996, *ARA&A*, 34, 607
 Tetarenko B., Dubus G., Lasota J.-P., Heinke C., Sivakoff G., 2018, *MNRAS*, 480, 2
 Tetarenko B. E., Sivakoff G. R., Heinke C. O., Gladstone J. C., 2016, *ApJS*, 222, 15
 Uemura M., Kato T., Pavlenko E., Shugarov S., Mitskevich M., Fried R. E., Sano Y., 2004, *PASJ*, 56, S147
 van Paradijs J., McClintock J. E., 1994, *A&A*, 290, 133
 Veledina A., Poutanen J., Vurm I., 2011, *ApJ*, 737, L17
 Whitehurst R., 1988, *MNRAS*, 232, 35
 Wijers R. A. M. J., Pringle J. E., 1999, *MNRAS*, 308, 207
 Woods D. T., Klein R. I., Castor J. I., McKee C. F., Bell J. B., 1996, *ApJ*, 461, 767
 Zdziarski A. A., Skinner G. K., Pooley G. G., Lubiński P., 2011, *MNRAS*, 416, 1324
 Zurita C. et al., 2002, *MNRAS*, 334, 999
 Życki P. T., Done C., Smith D. A., 2001, *MNRAS*, 326, 1367

This paper has been typeset from a $\text{\TeX}/\text{\LaTeX}$ file prepared by the author.